separations

MDPI

Article

Suitability of Hydrophilic and Hydrophobic Metal–Organic Frameworks as Porous Matrices for CO_2 Hydrate Formation

Xinyue Lu [1], Feng Chen [1], Fang Liu [1], Ying Teng [2,*], Hao Long [3], Zhao Liang [3,4], Ruiying Chen [1], Xiaxue Jiang [1], Dongyu An [1], Hairui Liang [1] and Pengfei Wang [2,3,*]

[1] CNOOC Key Laboratory of Liquefied Natural Gas and Low-Carbon Technology, Beijing 100028, China
[2] State Key Laboratory of Intelligent Construction and Healthy Operation and Maintenance of Deep Underground Engineering, Institute of Deep Earth Sciences and Green Energy, College of Civil and Transportation Engineering, Shenzhen University, Shenzhen 518060, China
[3] Advanced Institute for Ocean Research, Department of Physics, Institute of Major Scientific Facilities for New Materials, Southern University of Science and Technology, Shenzhen 518055, China
[4] School of Petroleum Engineering, China University of Petroleum (East China), Qingdao 266580, China
* Correspondence: tengying@szu.edu.cn (Y.T.); wangpf6@sustech.edu.cn (P.W.)

Abstract

Metal–organic frameworks (MOFs) offer tunable porous environments for hydrate-based CO_2 capture, yet their suitability depends on water accessibility and structural stability rather than surface area alone. This study investigated hydrophilic HKUST-1 and comparatively hydrophobic ZIF-8 using high-pressure differential scanning calorimetry (DSC), N_2 sorption, X-ray diffraction, and particle-size analysis. For HKUST-1, distinct CO_2 hydrate dissociation signals were detected at nominal pore-volume-based water loadings of 190% and 200%, but not at 50–150%. The corresponding dissociation conditions were 275.16 K/1.781 MPa and 271.90 K/1.590 MPa, respectively, indicating differences in thermal response without establishing an isobaric equilibrium shift. In contrast, ZIF-8 exhibited no detectable hydrate dissociation peaks under the investigated static powder-bed conditions, even with increased water loading or subcooling. Repeated thermal cycling in CO_2–water environments substantially reduced the accessible surface area of HKUST-1, whereas ZIF-8 retained its characteristic microporous adsorption behavior but exhibited pronounced particle agglomeration and structural changes. These findings highlight the coupled importance of water distribution, gas–water contact, and framework stability in evaluating MOFs for hydrate-based CO_2 capture.

Keywords: CO_2 hydrate; metal–organic frameworks; HKUST-1; ZIF-8; water loading; differential scanning calorimetry; cycling stability

Check for updates

Academic Editor: Manolis Manos

Received: 18 October 2026
Revised: 10 November 2026
Accepted: 15 November 2026
Published: 17 November 2026

Copyright: © 2026 by the authors. Licensee MDPI, Basel, Switzerland. This article is an open access article distributed under the terms and conditions of the Creative Commons Attribution (CC BY) license.

1. Introduction

Separating CO_2 from industrial gas streams remains important for emissions mitigation and carbon capture, utilization, and storage (CCUS) [1–3]. Capture routes differ in the energy and materials needed to deliver a concentrated CO_2 stream, and their suitability depends strongly on feed composition and operating pressure. Established processes include solvent absorption, solid adsorption, membranes, and low-temperature separation [4–9]. Hydrate-based separation provides a different route: selected guest molecules become incorporated in hydrogen-bonded water cages under appropriate pressure–temperature conditions [10–13]. CO_2 commonly forms structure-I hydrate [14]. In principle, selective hydrate formation may concentrate a guest gas, but its practical value depends on both the thermodynamic operating window and how quickly the gas and water are converted into hydrate. However, hydrate-

based CO_2 capture remains constrained by the energy requirements for gas compression and cooling, slow hydrate nucleation, and limited gas–water mass transfer [14,15].

CO_2 hydrate formation involves coupled gas transport, guest-molecule dissolution, nucleation, crystal growth, and heat transfer. Porous additives can influence these processes differently. Although the internal surfaces of MOFs may enhance local CO_2 adsorption, their micropores are not necessarily accessible to water or suitable for hydrate crystal growth. In hydrophilic frameworks, strong water–surface interactions may further alter water mobility and crystallization behavior. These effects are particularly relevant in powder beds, where hydrate formation may occur at particle surfaces and within interparticle voids rather than inside the intrinsic micropores. Consequently, the suitability of MOFs for hydrate formation depends on the accessibility and distribution of both CO_2 and water, in addition to their adsorption capacity and pore structure. High-pressure differential scanning calorimetry (DSC) provides information on the resulting thermal transitions, although the measured dissociation behavior may also depend on the imposed thermal history.

Thermodynamic additives, including tetrahydrofuran, tetra-n-butylammonium bromide, and cyclopentane, can modify hydrate stability, whereas agitation, surfactants, and dispersed solids commonly target formation kinetics [16–20]. Their benefits vary with the guest species and experimental conditions, and may be accompanied by increased process complexity, changes in gas occupancy, or difficult material recovery [21–24]. Porous matrices offer a potential alternative by redistributing water and guest molecules and providing solid–fluid interfaces. However, favorable behavior cannot be inferred from pore volume or adsorption capacity in isolation: surface chemistry, pore dimensions, bed packing, and the continuity of gas and water transport paths may act together or in opposition [25,26].

MOFs provide a useful platform for examining these interactions because their pore structures and surface chemistry are adjustable [27,28]. Previous studies have characterized hydrate behavior in MOF-containing systems, including CH_4 hydrate formation with ZIF-8 [29,30] and CO_2 hydrate phase behavior in MIL-53 [31]. However, these studies investigated different MOF structures, guest gases, or experimental configurations. The present study compares hydrophilic HKUST-1 and comparatively hydrophobic ZIF-8 in static CO_2–water powder beds, examining their hydrate-associated DSC responses under different water loadings and pressure–temperature conditions. The thermal results are further considered alongside changes in N_2-accessible porosity, particle-size distributions, and crystalline structure after repeated wet thermal exposure. This comparison provides a basis for evaluating MOF suitability beyond initial surface area and pore volume alone.

Here, initial porosity, crystallinity, and dispersed-particle size are characterized before high-pressure DSC measurements of water-loading, pressure, and minimum-temperature effects. Structural changes after repeated cooling–heating cycles are then examined by N_2 sorption, particle sizing, and X-ray diffraction (XRD). The analysis addresses three linked questions: under what loading conditions does a hydrate-associated thermal event become detectable; how do the observed events vary with imposed pressure–temperature paths; and which material properties remain accessible after cycling. The emphasis is on distinctions supported by the experimental evidence, with potential microscopic explanations kept separate from direct observations. This approach provides screening guidance without equating DSC peak detection with quantitative CO_2 uptake or separation selectivity.

2. Materials and Methods

2.1. Preparation of HKUST-1 and ZIF-8

HKUST-1 and ZIF-8 were selected as representative hydrophilic and hydrophobic MOFs, respectively. HKUST-1 was synthesized using a solvothermal method with $Cu(NO_3)_2{\cdot}3H_2O$ (99%, Shanghai Macklin Biochemical Co., Ltd., Shanghai, China) and

1,3,5-benzenetricarboxylic acid (98%, Shanghai Energy Chemical Technology Co., Ltd., Shanghai, China) as precursors, while ZIF-8 was prepared by a room-temperature stirring method using $Zn(NO_3)_2{\cdot}6H_2O$ (99%, Xilong Scientific Co., Ltd., Shantou, China) and 2-methylimidazole (99%, Shanghai Macklin Biochemical Co., Ltd., Shanghai, China) in methanol (99.5%, Shanghai Lingfeng Chemical Reagent Co., Ltd., Shanghai, China) [32–36]. All chemical reagents were purchased from Shanghai Aladdin Biochemical Technology Co., Ltd. (Shanghai, China). Detailed reagent information and synthesis procedures are provided in the Supplementary Materials (Section S1 and Figure S1).

2.2. Experimental Procedure

The as-prepared HKUST-1 and ZIF-8 samples were characterized by N_2 adsorption–desorption using an ASAP 2460 surface area and porosity analyzer (Micromeritics Instrument Corporation, Norcross, GA, USA), X-ray diffraction (XRD) using an Empyrean diffractometer (Malvern Panalytical B.V., Almelo, The Netherlands), and particle-size analysis using a NanoBrook 90Plus PALS analyzer (HORIBA Scientific, Kyoto, Japan). High-pressure differential scanning calorimetry (DSC) was performed using a BT2.15 Calvet-type calorimeter equipped with high-pressure vessels (SETARAM Instrumentation, Caluire, France) to examine thermal transitions at different water loadings, charging pressures, and minimum temperatures. The heat associated with each thermal transition was determined by integrating the corresponding baseline-corrected DSC endothermic peak. The integrated heat (Q, J) was reported for each transition. Where samples containing different amounts of water were compared, Q was normalized by the mass of added water to give q = Q/m(water) ($J{\cdot}g^{-1}$). This procedure was applied to both ice-melting and hydrate-dissociation peaks. Additional details of the material characterization methods are provided in the Supplementary Materials (Section S2).

Samples were initially held at 293.15 K for 0.5 h, cooled to the target temperature at 0.05 K min^{-1}, held for 5–6 h, and then heated to 293.15 K at the same rate. The selected pressures were 1.9–3.1 MPa, with additional tests at 5 MPa or a minimum temperature of 253.15 K for selected samples. The initial CO_2 charging pressure refers to the pressure established before the programmed temperature cycle. During cooling and subsequent heating, the system pressure varies with temperature and phase transitions. Therefore, the pressure recorded at an endothermic event is reported separately as the transition pressure and should not be confused with the initial charging pressure. Detailed high-pressure DSC protocols, experimental materials, and the representative apparatus and temperature program are provided in the Supplementary Materials (Section S3, Figure S2, and Table S1).

Both MOFs were also subjected to repeated cooling–heating tests at a nominal pore-volume-based water loading of 190%. In these tests, 500 mg of MOF was placed in a 10 mL reactor, charged with CO_2 to 2.8 MPa at 296 K, held for 30 min, cooled to 275.15 K for 10–11 h, and reheated to 296.15 K for 4 h. The recovered samples were dried and characterized after selected cycles. Further details of the cyclic stability tests and the representative temperature and pressure profiles are provided in the Supplementary Materials (Section S4 and Figure S3). DSC-derived transition temperatures are discussed as apparent dissociation temperatures rather than independently confirmed equilibrium temperatures [37]. DSC measurements were performed using a Setaram BT2.15 Calvet-type calorimeter with high-pressure vessels. The reproducibility of this instrument and protocol has been verified in our previous studies [37], with deviations of ±0.07 K in dissociation temperature and ±3.8 $J{\cdot}g^{-1}$ in q_{hyd}. Most conditions were measured once, and the 190% loading at approximately 2.5 MPa was measured in two independent experiments, giving consistent normalized dissociation heats (99.4 and 94.5 $J{\cdot}g^{-1}$). The results are therefore interpreted in terms of clearly resolved differences rather than statistically evaluated variations.

3. Results and Discussion

3.1. Initial Structure of the MOFs

The N_2 adsorption–desorption isotherms of HKUST-1 and ZIF-8 exhibit pronounced uptake at low relative pressures, confirming the predominantly microporous nature of both frameworks (Figure 1a). HKUST-1 shows a steep initial increase followed by a nearly constant adsorption capacity, consistent with rapid micropore filling. In contrast, ZIF-8 exhibits a more gradual increase in N_2 uptake over the investigated pressure range, suggesting differences in pore accessibility and adsorption behavior. The specific surface areas of HKUST-1 and ZIF-8 are 1305 and 1477 $m^2\ g^{-1}$, respectively, whereas their corresponding pore volumes are comparable at 0.55 and 0.56 $cm^3\ g^{-1}$ (Table 1). The pore-size distributions derived from the Horváth–Kawazoe method show characteristic peaks at approximately 0.46 nm for HKUST-1 and 0.90 nm for ZIF-8 (Figure 1b), indicating differences in their micropore structures [38].

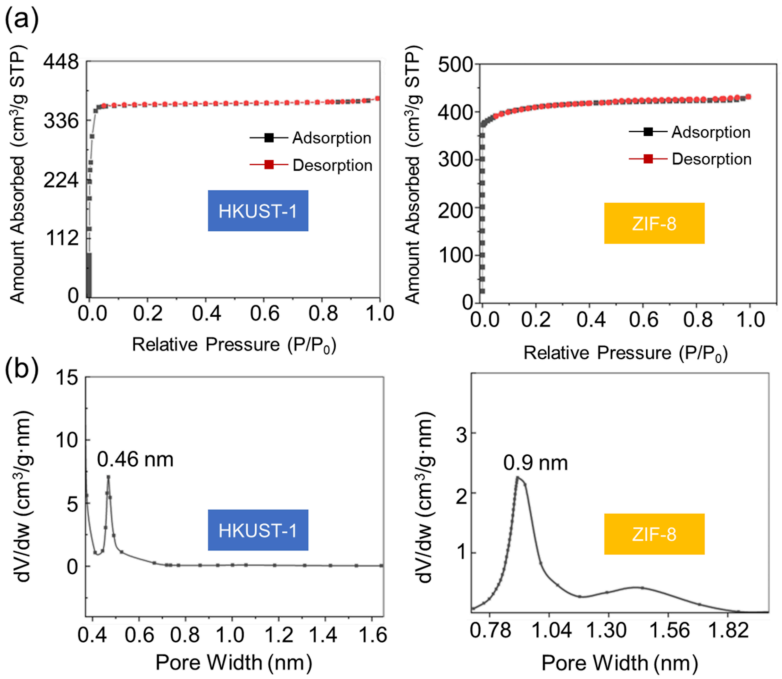


Figure 1. (**a**) N_2 adsorption–desorption isotherms; (**b**) pore-size distributions.

Table 1. Textural properties of the as-prepared MOFs.

Material	Surface Area (m^2/g)	Pore Size (nm)	Pore Volume (cm^3/g)
HKUST-1	1305	0.46	0.55
ZIF-8	1477	0.90	0.56

Although these textural properties are relevant to gas adsorption, their implications for hydrate formation require further consideration. The subnanometer pores characterized by N_2 adsorption may accommodate guest molecules but are too confined to support the growth of conventional three-dimensional CO_2 hydrate crystals. Hydrate formation is therefore more likely to involve water accessible at external particle surfaces, pore openings, and interparticle spaces. Moreover, the pore volume accessible to N_2 under dry measurement conditions does not necessarily represent the volume accessible to water under hydrate-forming conditions. Differences in surface wettability and water distribution

may consequently influence the availability of gas–water interfaces. Thus, despite its higher specific surface area, ZIF-8 cannot be assumed to provide more favorable conditions for CO_2 hydrate formation than HKUST-1.

The crystalline structures of the synthesized MOFs are shown in Figure 2a. HKUST-1 exhibits characteristic reflections at approximately 6.7°, 9.5°, 11.6°, 13.4°, and 19.0°, indexed to the (200), (220), (222), (400), and (440) planes, respectively. For ZIF-8, the prominent reflections at approximately 7.3°, 10.4°, 12.7°, 14.7°, and 18.0° correspond to the (011), (002), (112), (022), and (222) planes, respectively. These diffraction features agree with previously reported patterns [36,39], confirming the formation of the intended crystalline frameworks as the dominant phases. No prominent additional reflections are observed, although minor crystalline impurities or amorphous components cannot be excluded based on XRD alone.

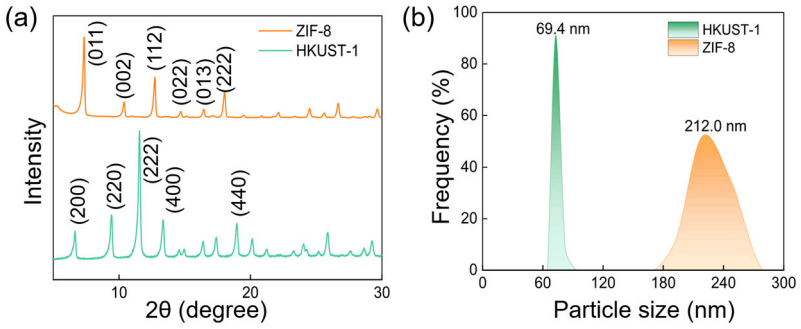


Figure 2. Structural and particle-size characterization of as-synthesized HKUST-1 and ZIF-8: (**a**) X-ray diffraction (XRD) patterns showing the characteristic diffraction reflections of the two crystalline frameworks; (**b**) particle-size distributions measured in aqueous dispersions, showing differences in apparent particle size and dispersion behavior. The measured particle sizes may include contributions from particle aggregation and do not necessarily represent the dimensions of individual MOF crystallites.

The particle-size distributions measured in aqueous dispersions are presented in Figure 2b. HKUST-1 shows a relatively narrow distribution centered near 69.4 nm, whereas ZIF-8 exhibits a broader distribution with a characteristic size of approximately 212 nm. The larger apparent particle size and broader distribution of ZIF-8 indicate differences in its dispersion behavior compared with HKUST-1. Because light-scattering measurements are sensitive to particle aggregation and dispersion conditions, these values should be interpreted as apparent particle sizes rather than the dimensions of individual MOF crystallites. Such differences may influence particle packing, interparticle voids, and the distribution of added water in the subsequent hydrate experiments. Together with the N_2 sorption results, these measurements establish the initial structural characteristics of the two MOFs and provide a reference for evaluating their changes after repeated thermal cycling.

3.2. DSC Observations of CO_2 Hydrate and Ice Transitions

3.2.1. Effect of Water Loading

Water loading plays an important role in determining the availability and distribution of water in porous materials during hydrate formation. In this study, water loading (S_v) was defined as the ratio of the volume of water added to the total pore volume of the dry MOF determined by N_2 adsorption, $S_v = V_{water}/(mMOF_{vp}) \times 100\%$, where mMOF and vp represent the dry MOF mass and specific pore volume, respectively. This parameter provides a consistent basis for specifying the amount of water introduced into each system and should not be interpreted as the actual fraction of micropores occupied by water. At nominal loadings above 100%, the added water volume exceeds the N_2-accessible pore volume, and

the excess water is accommodated on external particle surfaces and in interparticle spaces. Although HKUST-1 and ZIF-8 have similar measured pore volumes (0.55 and 0.56 cm^3/g, respectively), their different affinities for water can result in different water distributions at the same nominal loading. Therefore, comparisons between the two MOFs are made on the basis of the water added relative to their dry-state pore volumes, rather than assuming identical internal pore saturation or gas–water contact conditions.HKUST-1 was examined at water loadings of 50%, 120%, 150%, 190%, and 200%, with an initial CO_2 pressure of approximately 2.5 MPa.

The DSC curves reveal a pronounced dependence of the observed phase transitions on water loading (Figure 3a). At loadings of 50–150%, the heating curves exhibit ice-associated melting features without a clearly resolved CO_2 hydrate dissociation peak. In contrast, additional endothermic features attributed to hydrate dissociation appear at 190% and 200%, indicating that sufficiently high water loading favors detectable hydrate formation under the investigated conditions. At lower loadings, part of the introduced water may be retained near hydrophilic framework surfaces or within confined regions, reducing the amount of water available at accessible gas–liquid interfaces. Increasing the water inventory can facilitate the development of more extensive water-containing regions between particles, potentially improving contact between CO_2 and water. The emergence of hydrate-associated signals at higher loadings is therefore consistent with improved water availability, although the DSC results do not establish a unique critical saturation for hydrate nucleation.

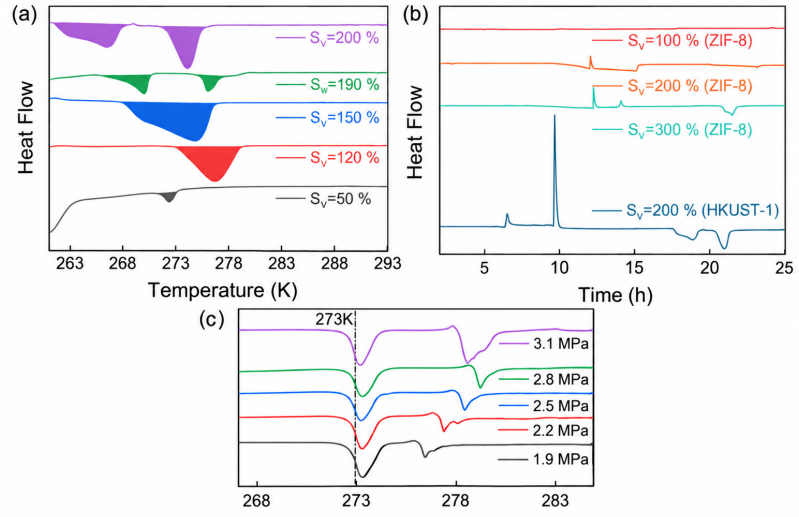


Figure 3. Comparison of thermal traces: (**a**) HKUST-1 at different water loadings; (**b**) ZIF-8 and HKUST-1; (**c**) bulk-water reference at different pressures.

The ice-associated melting temperatures also vary with water loading (Table 2). The measured values are 271.1, 272.0, 267.43, 267.67, and 263.14 K at nominal loadings of 50%, 120%, 150%, 190%, and 200%, respectively. Despite minor non-monotonic variations, the overall response shows lower apparent melting temperatures at higher water loadings. This behavior may reflect changes in the distribution and local environment of freezable water, including contributions from surface-associated water and water confined within interparticle regions. However, the pressure at the measured transition also varies among samples, and the temperature differences cannot be attributed solely to pore confinement. In addition, the extent to which water occupies intrinsic micropores or external interparticle spaces cannot be determined from the melting temperatures alone.

For the samples without a resolved hydrate dissociation feature, the integrated ice-melting heat ($Q_{m(ice)}$) increased from 43.13 J at 50% loading to 194.56 and 240.91 J at 120%

and 150%, respectively (Table 2). This increase indicates a larger ice-melting thermal response as more water is introduced, consistent with an increase in the amount of water participating in detectable freezing and melting transitions. However, the integrated heat also depends on the peak integration procedure and may include contributions from other thermal effects, so it is interpreted as a change in the ice-associated thermal response rather than direct evidence of differences in ice fraction or crystallinity.

Table 2. Ice-related DSC observations at different water loadings.

$M_{HKUST-1}$/mg	M_{H2O}/mg	Water Loading (%)	$T_{m(ice)}$/K	$P_{m(ice)}$/MPa	$Q_{m(ice)}$/J
741.75	205.45	50%	271.25	2.00	43.13
711.71	474.08	120%	272.15	1.81	194.56
751.83	625.91	150%	267.58	1.60	240.91
722.15	740.54	190%	267.82	1.78	28.85
752.13	834.87	200%	263.29	1.65	74.90

At higher water loadings, hydrate-associated dissociation features were detected at 275.16 K and 1.781 MPa for 190% loading and at 271.90 K and 1.590 MPa for 200% loading (Table 3). Although the measured temperatures differ by 3.26 K, the corresponding pressures also differ by 0.191 MPa. The corresponding hydrate-associated heats ($Q_{hydrate}$) were 73.63 and 67.61 J, or 99.4 and 81.0 $J \cdot g^{-1}$ after normalization by the mass of added water. The available measurements do not establish whether this difference arises from changes in hydrate quantity, thermal response, or experimental variability. The principal finding is that hydrate-associated transitions become detectable at the two highest water loadings, whereas the lower-loading samples show no distinct corresponding feature under the same experimental protocol.

Table 3. Hydrate-associated DSC observations for HKUST-1 at different water loadings.

$M_{HKUST-1}$/mg	M_{H2O}/mg	Water Loading (%)	T/K	P/MPa	$Q_{hydrate}$/J
741.75	205.45	50%	—	—	—
711.71	474.08	120%	—	—-	—
751.83	625.91	150%	—	—	—
722.15	740.54	190%	275.16	1.781	73.63
752.13	834.87	200%	271.90	1.590	67.61

The dependence on water loading can be interpreted in terms of the competition between water availability and gas accessibility within the HKUST-1 powder bed (Figure 4). At low loading, water may preferentially occupy strongly interacting surface regions and localized interparticle contacts, leaving a limited volume of connected water accessible to CO_2. As loading increases, more continuous water-containing regions may develop around particle surfaces and between adjacent particles, providing additional locations for hydrate nucleation and growth. Further water addition may increase the thickness or extent of external liquid regions and alter CO_2 transport pathways. These effects suggest that increasing water loading does not necessarily improve hydrate formation in direct proportion to the amount of added water. Instead, the resulting thermal response reflects the combined influence of water availability, gas–water contact, and transport within the particle assembly. The distributions illustrated in Figure 4 represent possible configurations rather than directly observed microstructures.

The behavior of ZIF-8 differs substantially from that of HKUST-1. As shown in Figure 3b, no distinct CO_2 hydrate dissociation peak was detected in ZIF-8 at water loadings of 100%, 200%, or 300%. Only weak thermal signals were observed at higher loadings, indicating limited detectable phase-transition activity under the present static powder-bed conditions. Although ZIF-8 has a slightly higher specific surface area than HKUST-1, its comparatively hydrophobic surface may restrict water penetration into microporous regions and favor a different distribution of water among external particle surfaces and interparticle voids. Consequently, CO_2 adsorption sites and water-accessible regions may not coincide sufficiently to support appreciable hydrate formation during the experimental period. This interpretation is consistent with the contrasting DSC responses, although the spatial distributions of CO_2 and water were not directly measured.

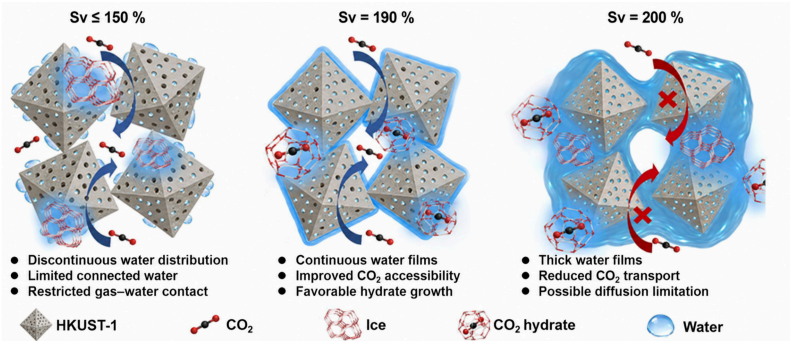


Figure 4. Conceptual illustration of possible water distribution and gas-access pathways in HKUST-1 powder beds at different nominal water loadings (Arrows indicate the schematic CO_2 transport pathways, while red crosses denote restricted or blocked CO_2 transport).

Previous studies have reported enhanced CH_4 hydrate formation in ZIF-8-containing aqueous dispersions and emulsions [40,41]. Unlike the static powder-bed configuration investigated here, dispersed systems provide different particle–liquid contact conditions and may increase the availability of heterogeneous nucleation interfaces. Differences in guest-gas properties and experimental conditions further complicate direct comparisons. Therefore, the present results do not establish an intrinsic inhibitory effect of ZIF-8 on hydrate formation, but indicate that its performance depends strongly on the accessibility and arrangement of gas and water within the reaction system.

Overall, the contrasting responses of HKUST-1 and ZIF-8 demonstrate that the effectiveness of a MOF as a hydrate-forming matrix cannot be assessed solely from its specific surface area or micropore volume. The distribution of water and its accessibility to CO_2 within the particle assembly are equally important considerations.

3.2.2. Effect of Pressure

Pressure is an important factor governing CO_2 hydrate stability and formation behavior. Its influence was examined in HKUST-1 at water loadings of 190% and 200%, with initial CO_2 pressures ranging from 1.9 to 3.1 MPa. As shown in Figure 5a,b, both ice-melting and hydrate-associated dissociation peaks are observed at initial CO_2 pressures of 1.9–2.5 MPa. At higher pressures (2.8–3.1 MPa), the ice-melting peaks become less pronounced or are no longer clearly resolved, while hydrate-associated dissociation peaks remain detectable. The reduction or disappearance of a distinct ice-melting peak at higher pressures is consistent with a change in the relative amounts of ice and hydrate formed during cooling. Higher CO_2 pressure generally favors hydrate stability and increases the thermodynamic driving force for formation at a given temperature, potentially allowing a larger fraction of the available water to participate in hydrate formation. Nevertheless, the measured heating

response also depends on the preceding cooling and holding stages. The pressure values of 1.9–3.1 MPa used to compare the DSC experiments refer to the initial CO_2 charging pressures. By contrast, the pressures listed alongside the thermal transition temperatures represent the measured pressures at the corresponding endothermic events. This distinction is particularly important for Figure 5d, where the plotted pressure–temperature points describe apparent hydrate dissociation conditions rather than the initial experimental settings.

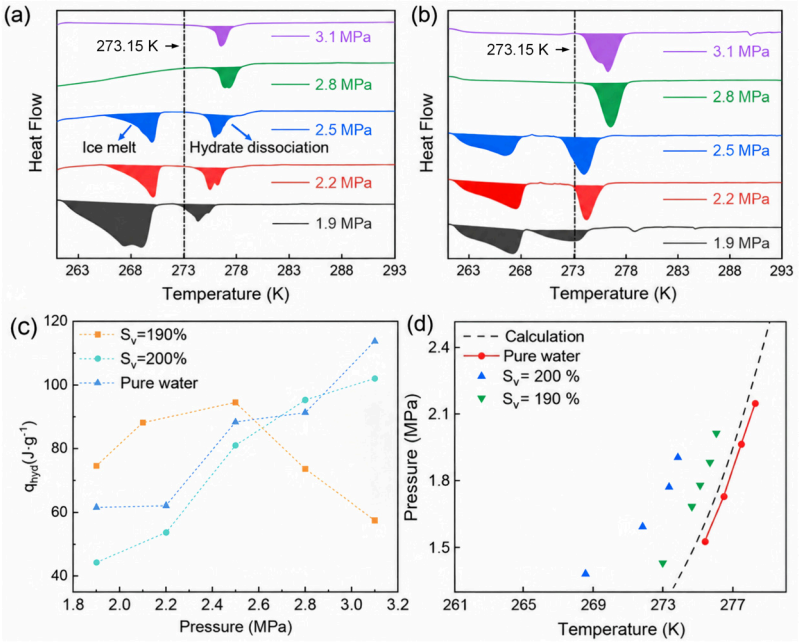


Figure 5. Effects of CO_2 charging pressure on the thermal behavior of HKUST-1 at different nominal water loadings: DSC heating curves at (**a**) 190% and (**b**) 200% water loading; (**c**) hydrate-associated dissociation heat normalized by the mass of added water (q_{hyd}) as a function of charging pressure; and (**d**) apparent hydrate dissociation conditions compared with the bulk-water reference. Sample compositions: 190%, HKUST-1 215.2 mg and water 225.2 mg; 200%, HKUST-1 752.13 mg and water 834.87 mg; bulk-water reference, water 250 mg.

The pressure dependence of the thermal response differs between the two water loadings. Because the samples contained different amounts of water, the integrated heats were normalized by the mass of added water. As the initial CO_2 pressure increased from 1.9 to 2.5 MPa, the q_{ice} decreased from 158.7 to 128 J·g^{-1} at 190% loading and from 112.0 to 89.7 J·g^{-1} at 200% loading (Table 4). Over the same pressure range, q_{hyd} increased from 74.6 to 94.5 J·g^{-1} and from 44.3 to 81.0 J·g^{-1}, respectively (Figure 5c). These opposing trends are consistent with increased hydrate formation at the expense of ice formation during cooling, although quantitative phase fractions cannot be determined without accounting for the distinct transition enthalpies.

At higher charging pressures (2.8–3.1 MPa), the two loadings showed different trends (Figure 5c). At 200% loading, q_{hyd} continued to increase to 102.0 J·g^{-1} at 3.1 MPa, whereas at 190% loading it reached a maximum of 94.5 J·g^{-1} at 2.5 MPa and decreased to 57.5 J·g^{-1} at 3.1 MPa. This contrast suggests that the pressure dependence of the hydrate-associated response is related to water loading, possibly through differences in water availability and gas–water contact within the powder bed. Relative to the bulk-water reference (61.6–113.7 J·g^{-1}), q_{hyd} for HKUST-1 was higher at 190% loading under low pressures (1.9–2.2 MPa) but lower or comparable under other conditions, indicating no consistent enhancement of the hydrate-associated heat per unit mass of water. The peak heats alone cannot distinguish changes in hydrate quantity from differences in thermal history.

Table 4. Ice-related DSC observations at two water loadings; pressure and transition pressure are distinguished.

Water Loading (%)	P/MPa	$T_{m(ice)}$/K	$P_{m(ice)}$/MPa	$Q_{m(ice)}$/J
190%	1.9	263.28	2.01	35.73
	2.1	267.93	1.67	30.77
	2.5	267.82	1.78	28.85
200%	1.9	261.56	1.41	93.47
	2.2	261.55	1.61	85.72
	2.5	263.29	1.65	74.90

Figure 5d compares the measured hydrate-associated dissociation conditions in HKUST-1 with the bulk-water CO_2 hydrate reference [42]. The HKUST-1 data deviate from the reference pressure–temperature relationship, indicating that the thermal response differs between the MOF-containing and bulk-water systems. Such differences may arise from the heterogeneous water environment, possible confinement-related effects, and the thermal history imposed during DSC measurements. However, because the transition points were obtained from dynamic heating scans, they represent apparent dissociation conditions rather than independently established thermodynamic equilibrium states. Distinguishing a genuine equilibrium shift from kinetic and measurement-related contributions would require additional equilibrium-confirmation experiments. The observed differences should therefore not be interpreted as quantitative evidence of thermodynamic inhibition by HKUST-1.

Additional experiments were conducted at a CO_2 pressure of 5 MPa to examine whether increased pressure produced detectable hydrate-related transitions in samples that showed weak or absent signals at lower pressures (Figure 6). HKUST-1 at 120% water loading exhibited more pronounced thermal events, whereas ZIF-8 showed no clearly resolved hydrate dissociation feature at the investigated water loadings. This contrast suggests that increasing pressure alone did not overcome the limitations associated with the tested ZIF-8 powder-bed configuration. Some thermal features observed during cooling may also involve CO_2 phase transitions, although their assignment requires consideration of the actual pressure–temperature trajectory. Together, these observations indicate that pressure and water loading jointly affect the detectable hydrate-related response, while the influence of the porous matrix cannot be inferred from pressure dependence alone.

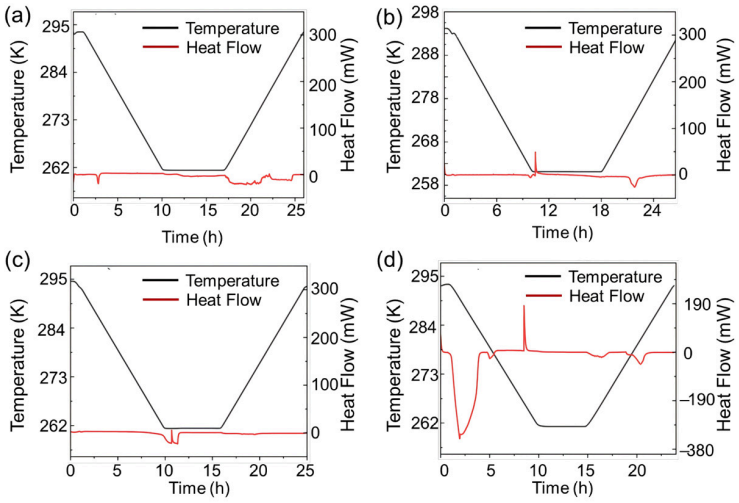


Figure 6. Temperature profiles and corresponding DSC heat-flow responses of MOF–water samples at an initial CO_2 charging pressure of 5 MPa: ZIF-8 at nominal water loadings of (**a**) 100%, (**b**) 200%, and (**c**) 300%, and (**d**) HKUST-1 at 120%.

3.2.3. Effect of Minimum Temperature

To examine whether deeper cooling could induce detectable hydrate formation at lower water loadings, the minimum temperature was reduced from 261.15 to 253.15 K while maintaining an initial CO_2 pressure of 2.5 MPa. For HKUST-1 at nominal water loadings of 50%, 120%, and 150%, lowering the minimum temperature altered the position and shape of the endothermic features observed during subsequent heating (Figure 7). The changes were particularly evident at 120% and 150% loading, where relatively broad melting-related peaks were observed. However, no additional, clearly distinguishable hydrate dissociation peak emerged at 253.15 K. These observations indicate that deeper cooling affected the thermal behavior of the water-containing samples without producing a detectable increase in hydrate-associated phase transitions under the applied protocol.

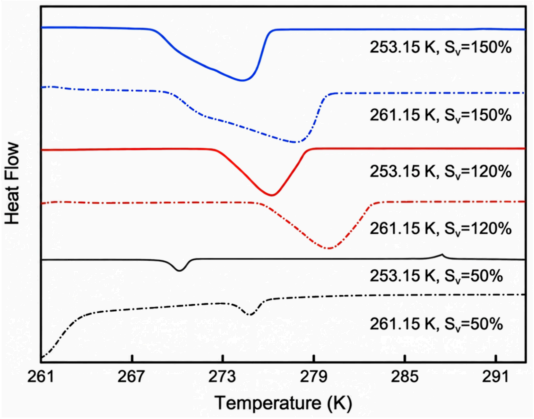


Figure 7. Effect of minimum temperature (253.15 and 261.15 K) on the DSC heating traces of HKUST-1 at nominal water loadings of 50%, 120%, and 150%.

The ZIF-8 samples exhibited a different thermal response (Figure 8a–c). Although the 100% loading showed only minor heat-flow variations, more pronounced thermal events occurred at 200% and 300% loading during cooling and subsequent heating. The sharp exothermic features may reflect rapid crystallization or other phase transitions, but their origin cannot be established from heat-flow signals alone. Similarly, the thermal response of HKUST-1 at 120% loading (Figure 8d) confirms that reducing the minimum temperature can alter the sequence and intensity of thermal events without necessarily generating a distinct hydrate dissociation signature. Thus, the absence of an identifiable hydrate peak in these experiments should not be interpreted as a general insensitivity of either MOF system to temperature.

The limited hydrate-related response despite deeper cooling may arise from competing effects of temperature on hydrate formation and water freezing. Lower temperatures can increase the thermodynamic driving force for CO_2 hydrate formation, but earlier or more extensive ice formation may reduce the amount of mobile liquid water available for hydrate growth. Once ice occupies part of the accessible water-containing regions, subsequent hydrate formation may become increasingly dependent on gas transport and the remaining unfrozen water. Under the present finite holding period, these competing processes could limit the appearance of detectable hydrate dissociation peaks. Therefore, reducing the minimum temperature alone did not substantially improve the detectable hydrate response at the investigated lower water loadings, emphasizing the importance of the imposed thermal pathway rather than minimum temperature alone.

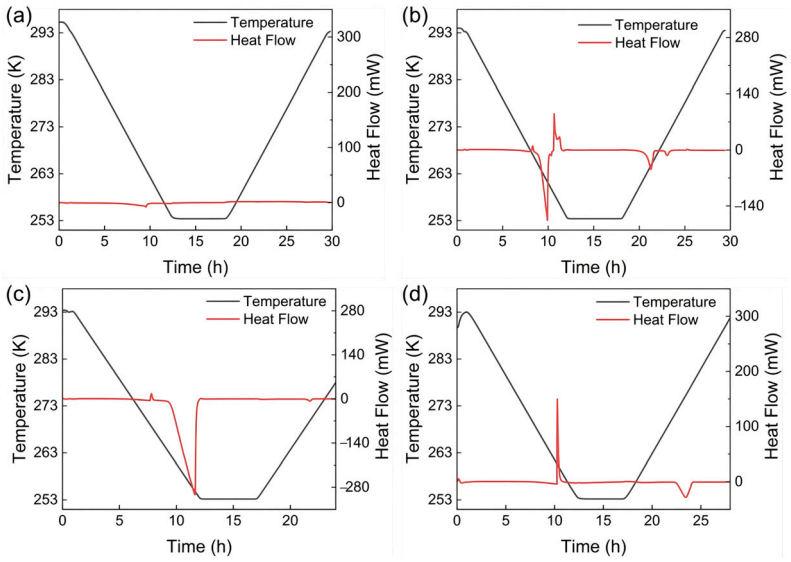


Figure 8. Temperature profiles and corresponding DSC heat-flow responses during cooling–heating experiments with a minimum temperature of 253.15 K: ZIF-8 at nominal water loadings of (**a**) 100%, (**b**) 200%, and (**c**) 300%, and (**d**) HKUST-1 at 120%.

3.3. Structural Changes After Repeated Thermal Cycling

The structural stability of HKUST-1 and ZIF-8 was evaluated after repeated cooling–heating cycles in a CO_2–water environment at a nominal water loading of 190%. The recovered materials were dried and degassed at 393.15 K for 7 h before N_2 adsorption measurements at 77.15 K. As shown in Figures 9 and 10, both MOFs exhibited changes in their adsorption behavior, although the extent and nature of these changes differed considerably. For HKUST-1, the initially micropore-filling behavior was weakened after cycling, accompanied by the development of adsorption–desorption hysteresis at intermediate and high relative pressures (Figure 9). This combination suggests a loss of accessible microporosity and an increased contribution from larger pores or interparticle voids. In contrast, ZIF-8 retained the steep low-pressure uptake characteristic of microporous materials, with relatively limited hysteresis throughout the investigated cycles (Figure 10). These differences indicate that the two frameworks respond differently to repeated exposure to water and CO_2 under the applied thermal conditions.

The evolution of specific surface area further illustrates this contrast (Figure 11a). HKUST-1 exhibited a pronounced decrease from its initial value of 1305 $m^2\ g^{-1}$ to approximately 350 $m^2\ g^{-1}$ after the first cycle, with relatively small additional changes during subsequent cycles. The substantial initial loss suggests that the first exposure to the cycling environment accounts for much of the reduction in N_2-accessible porosity.

The decrease in the N_2-accessible surface area of HKUST-1 indicates that most of the measured loss in pore accessibility occurred during the initial exposure to the CO_2–water environment (Figure 11a). This reduction was accompanied by weakened micropore-filling behavior and pronounced adsorption–desorption hysteresis (Figure 9), indicating changes in the accessible pore network. Meanwhile, several characteristic XRD reflections remained identifiable after cycling, although their intensities changed (Figure 12c). The contrasting responses reflect the different structural characteristics probed by these techniques. XRD detects crystalline order in the remaining diffracting regions, whereas N_2 adsorption depends on the accessibility of internal pore surfaces. Consequently, recognizable diffraction features can persist despite a substantial reduction in accessible microporosity. Water-induced local structural alteration and partial pore blockage may contribute to this behavior, consistent with previous studies on the water sensitivity and surface defects of HKUST-1 [43–45].

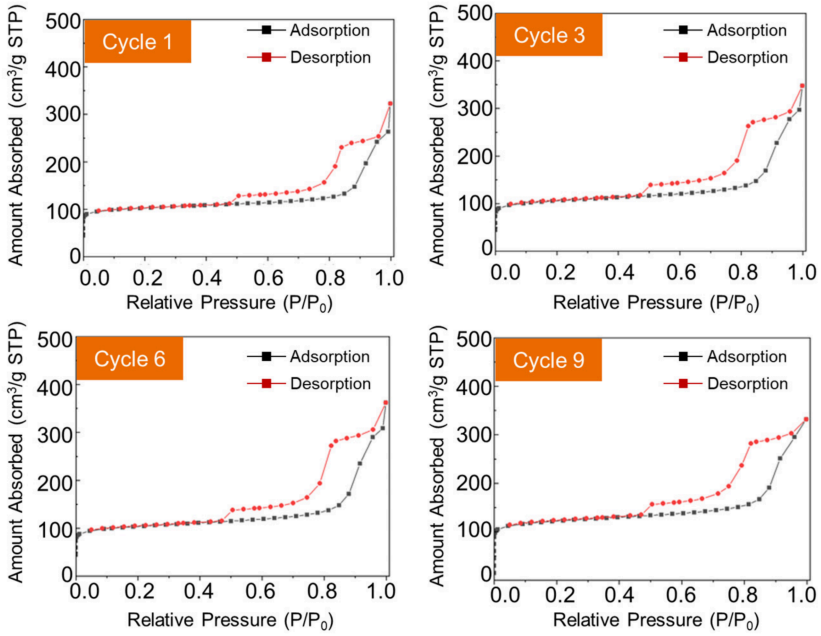


Figure 9. N_2 adsorption–desorption isotherms of HKUST-1 after 1, 3, 6, and 9 thermal cycles.

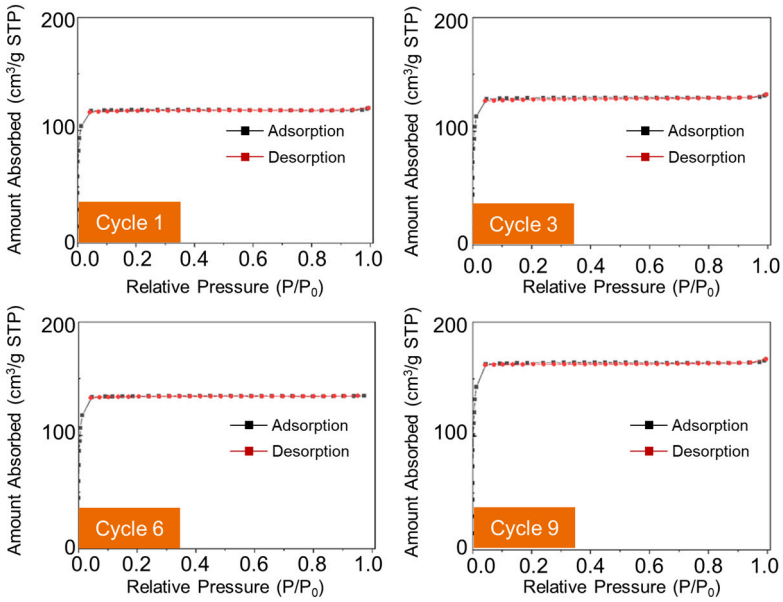


Figure 10. N_2 adsorption–desorption isotherms of ZIF-8 after 1, 3, 6, and 9 thermal cycles.

The N_2 sorption-derived pore-width distributions provide further evidence of changes in the accessible pore network, showing increased contributions from larger spaces in the mesopore-size range after cycling (Figure 11b). Together with the reduced micropore-filling response, this observation indicates a redistribution of N_2-accessible pore space rather than a uniform reduction in adsorption across all pore sizes. The apparent particle size of HKUST-1 also increased from approximately 69.4 to 280 nm over nine cycles (Figure 12a), indicating changes in particle dispersion or aggregation. However, the substantial BET surface-area loss occurred predominantly after the first cycle, whereas the reported particle-size increase describes the overall evolution over nine cycles. Moreover, an increase in apparent particle size does not directly quantify changes in intrinsic micropore accessibility. These results therefore indicate that particle aggregation alone is insufficient to explain the observed reduction in BET surface area. Local framework alteration, restricted pore access, and

changes in interparticle voids remain possible contributors, although their individual effects cannot be resolved from the available measurements.

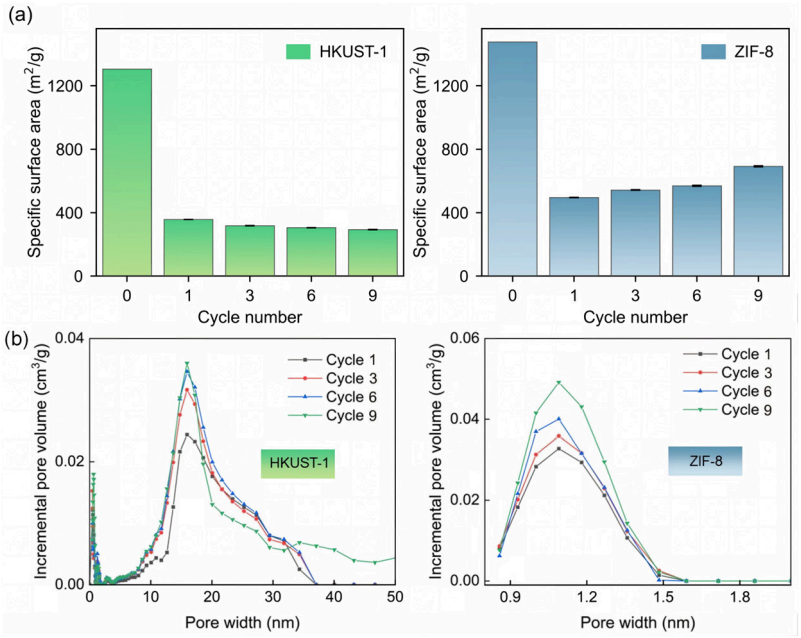


Figure 11. Evolution of (**a**) specific surface area and (**b**) N_2 sorption-derived pore-width distributions of HKUST-1 and ZIF-8 during thermal cycling. Error bars in (**a**) represent the standard error of the BET linear regression.

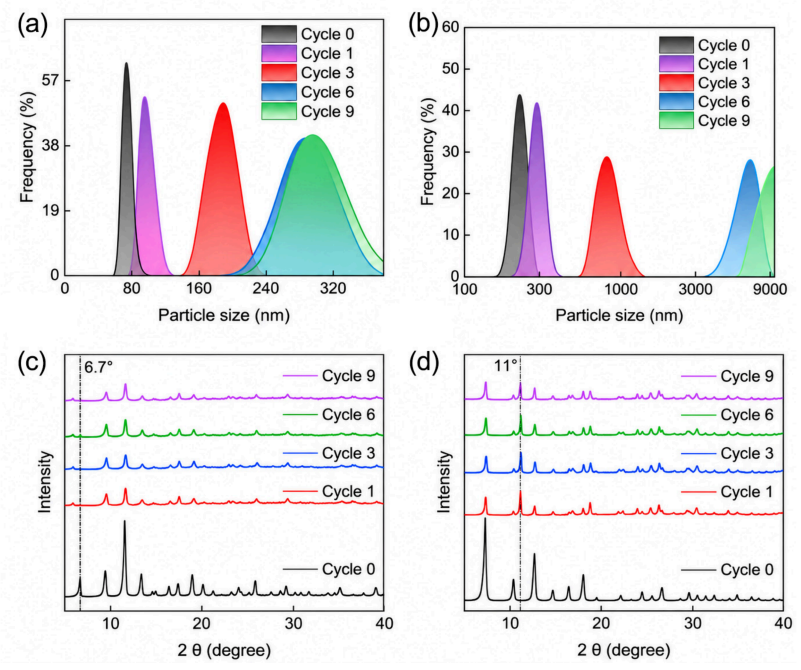


Figure 12. Changes in particle-size distributions of (**a**) HKUST-1 and (**b**) ZIF-8, and XRD patterns of (**c**) HKUST-1 and (**d**) ZIF-8 after different numbers of thermal cycles.

ZIF-8 showed a different trend, with a substantial initial decrease in BET surface area followed by a gradual increase over the subsequent measured cycles (Figure 11a). This partial recovery may reflect changes in the accessibility of the remaining microporous network, as the N_2 adsorption–desorption isotherms retained characteristic low-pressure uptake throughout cycling (Figure 10). However, the increase in measured surface area

does not necessarily indicate restoration of the original framework, particularly given the particle agglomeration and changes in XRD features observed after cycling (Figure 12). Previous studies have also reported irreversible structural changes in ZIF-8 exposed to CO_2 and water [46]. The underlying cause and reproducibility of the observed surface-area increase cannot be established from the present measurements.

Particle-size analysis provides complementary evidence of changes in the physical organization of the MOF powders (Figure 12a,b). Both materials exhibited an increase in apparent particle size with increasing cycle number. Such pronounced growth in apparent particle size is more consistent with aggregation or agglomeration than with the growth of individual MOF crystallites. Repeated wetting, drying, and changes in interparticle contact may contribute to the formation of larger particle assemblies. Notably, the increase in apparent particle size of ZIF-8 occurred alongside partial recovery of its measured surface area. This indicates that particle aggregation and micropore accessibility may evolve independently: the formation of larger aggregates does not necessarily eliminate access to all internal micropores. Although aggregation may alter interparticle packing and transport pathways, the observed particle-size changes do not establish a direct contribution to the pronounced loss of intrinsic micropore surface area.

The XRD patterns provide further insight into changes in crystalline structure (Figure 12c,d). For HKUST-1, the characteristic reflection near 6.7° became substantially weaker or less distinguishable after cycling, while changes in the intensities of other reflections were also observed (Figure 12c). These observations suggest alterations in crystalline order or the relative contribution of the original framework phase, although the extent of structural degradation cannot be quantified from the present diffraction data. Together with the substantial loss of N_2-accessible surface area, these observations suggest changes in the porous structure while recognizable crystalline regions remain present. Local structural defects and reduced accessibility at pore entrances provide possible explanations, although the present measurements do not establish the specific chemical changes or the extent of framework degradation.

For ZIF-8, several characteristic diffraction reflections remained identifiable after cycling, although their relative intensities changed and an additional diffraction feature appeared near 11° (Figure 12d). These observations suggest possible changes in crystalline order, framework structure, or phase composition rather than complete preservation of the original crystalline framework. However, the available XRD data do not establish the extent of these changes or identify the origin of the additional diffraction feature. Formation of zinc-containing secondary phases in a CO_2–water environment is possible [46,47], but the available diffraction evidence is insufficient to establish a specific product. The combined XRD and N_2 sorption results indicate that ZIF-8 retains more recognizable features of its original crystalline and microporous structure than HKUST-1 after cycling, although both materials exhibit structural changes under the investigated conditions.

Taken together, the results reveal distinct modes of material change during repeated thermal cycling. HKUST-1 undergoes a substantial loss of accessible microporosity accompanied by changes in its diffraction characteristics, whereas ZIF-8 retains recognizable microporous adsorption and diffraction features but exhibits pronounced particle agglomeration. These findings indicate that structural stability in hydrate-forming environments cannot be evaluated from specific surface area alone. Retention of crystalline order, accessibility of internal pores, and stability of particle assemblies are complementary considerations when assessing the suitability of MOFs for repeated use in hydrate-based CO_2 capture processes.

3.4. Implications for Hydrate-Based CO_2 Capture

The contrasting behavior of HKUST-1 and ZIF-8 highlights the need to evaluate porous materials for hydrate-based CO_2 capture beyond their initial gas adsorption properties. Although both MOFs possess high specific surface areas and comparable pore volumes, their hydrate-associated thermal responses and structural changes during cycling differ substantially. HKUST-1 exhibits detectable hydrate dissociation features at higher water loadings but undergoes a pronounced loss of accessible microporosity after repeated exposure to CO_2-rich water. In contrast, ZIF-8 retains a more recognizable microporous structure while showing no clearly resolved hydrate dissociation signal under the investigated static powder-bed conditions and considerable particle agglomeration after cycling. These results indicate that gas adsorption capacity, accessibility of water to CO_2, and structural durability represent distinct but interconnected considerations in assessing MOFs for hydrate-based applications.

From a material-design perspective, an effective porous matrix should provide accessible gas–water contact regions while maintaining sufficient transport pathways and structural integrity during repeated operation. Its suitability therefore depends not only on intrinsic pore characteristics and surface wettability but also on the arrangement of particles and the distribution of water under operating conditions. This distinction is particularly relevant when translating material properties measured under dry adsorption conditions to hydrate-forming environments. The industrial application of these MOFs in hydrate-based CO_2 capture also faces several practical challenges. Gas compression and cooling are required to establish suitable hydrate-forming conditions, and their energy demands must be considered alongside hydrate formation and dissociation processes. Although increasing CO_2 pressure affected the thermal responses in the present experiments, no clearly resolved hydrate dissociation features were observed in ZIF-8 under the investigated conditions, indicating that increasing pressure alone was insufficient to produce a detectable hydrate dissociation response under the investigated conditions. Moreover, the static DSC measurements do not directly establish hydrate nucleation rates, growth kinetics, or CO_2 capture productivity. These factors are particularly important for continuous operation, where rapid hydrate formation and efficient gas–liquid contact are required. In addition, practical CO_2 separation involves multicomponent gas streams, whereas the present experiments used CO_2 without competing gas species. Consequently, CO_2 selectivity, recovery efficiency, and product purity remain undetermined. Together with the structural changes observed after thermal cycling, these considerations indicate that material suitability must be assessed in conjunction with process energy requirements, formation kinetics, separation performance, and long-term durability [12].

Although the cycling experiments provide insight into the structural durability of the MOFs, hydrate-associated DSC responses were not evaluated for the recovered samples after successive cycles. Therefore, changes in hydrate formation performance and material reusability cannot be established from the structural characterization results alone. Further evaluation should combine repeated hydrate formation measurements with quantitative CO_2 uptake and hydrate conversion analysis to establish the relationship between performance retention and structural changes, including possible changes in pore accessibility and framework integrity. The present findings provide a material-level basis for further evaluation by highlighting the limitations of relying on initial microporosity or specific surface area alone when selecting MOFs for hydrate-based CO_2 capture.

4. Conclusions

This study compared hydrophilic HKUST-1 and comparatively hydrophobic ZIF-8 as porous matrices for CO_2 hydrate formation, focusing on their hydrate-associated thermal

responses and structural changes during repeated thermal cycling. For HKUST-1, distinct hydrate-associated DSC dissociation peaks were observed at nominal water loadings of 190% and 200%, but not at 50–150%. The corresponding dissociation conditions were 275.16 K/1.781 MPa and 271.90 K/1.590 MPa, respectively. These measurements represent apparent dissociation conditions rather than independently established equilibrium states. In contrast, ZIF-8 exhibited no clearly resolved hydrate dissociation peaks under the investigated static powder-bed conditions.

Thermal cycling produced different structural responses in the two MOFs. The N_2-accessible surface area of HKUST-1 decreased from 1305 to approximately 350 m^2/g after the first cycle, accompanied by changes in its adsorption behavior and XRD reflections. ZIF-8 retained recognizable microporous adsorption characteristics but exhibited substantial particle agglomeration and changes in diffraction features. These observations are consistent with possible framework alteration and changes in pore accessibility, although the underlying mechanisms could not be independently established.

The findings demonstrate that initial specific surface area and microporosity alone are insufficient to assess MOF suitability for hydrate-based CO_2 capture. Water accessibility, gas–water contact, and structural durability are also important considerations. However, quantitative CO_2 uptake, hydrate formation performance after repeated use, and gas separation selectivity remain undetermined. Further evaluation of these parameters is necessary to establish the practical applicability of these materials.

Supplementary Materials: The following supporting information can be downloaded at: https://www.mdpi.com/article/10.3390/separations13110344/s1: Figure S1: Schematic of the HKUST-1 and ZIF-8 preparation procedures; Figure S2: (a) High-pressure DSC apparatus and (b) representative temperature program and heat-flow response. Thermal-event labels indicate tentative peak assignments, not independently verified phase equilibria; Table S1: Materials; Figure S3: (a) Experimental apparatus for repeated CO_2–water thermal cycling and (b) representative temperature and pressure profiles during cycling.

Author Contributions: Conceptualization, X.L. and F.C.; Methodology, F.L. and R.C.; Validation, X.J., D.A. and H.L. (Hairui Liang); Formal analysis, Z.L., X.J. and D.A.; Investigation, F.L., H.L. (Hao Long) and R.C.; Data curation, Y.T.; Writing—original draft, X.L., F.C., F.L., Y.T., H.L. (Hao Long), Z.L., R.C., X.J., D.A., H.L. (Hairui Liang) and P.W.; Writing—review & editing, P.W.; Supervision, P.W.; Project administration, P.W.; Funding acquisition, Y.T. All authors have read and agreed to the published version of the manuscript.

Funding: This work was primarily supported by the Open Fund Project 202619839897, Key Laboratory of Liquefied Natural Gas and Low-Carbon Technology, CNOOC, the National Natural Science Foundation of China (52676150, 52674126 and 52304098); the Natural Science Foundation of Guangdong Province (2025A1515010748); the State Key Laboratory of Intelligent Construction and Healthy Operation and Maintenance of Deep Underground Engineering (SDQZK2631); and the Youth Science and Technology Talent Support Programme of the Guangdong Provincial Association for Science and Technology.

Data Availability Statement: The original contributions presented in this study are included in the article/Supplementary Materials. Further inquiries can be directed to the corresponding authors.

Acknowledgments: We thank Shenzhen Guangming Science City Development and Construction Co., Ltd. and its Material Genome Big-Science Facilities Platform for providing technical support and assistance in data collection and analysis, and the High-Pressure Neutron Diffractometer (https://cstr.cn/31113.02.CSNS.HPND, accessed on 1 September 2026) operated by Southern University of Science and Technology and China Spallation Neutron Source (CSNS) (https://cstr.cn/31113.02.CSNS, accessed on 1 September 2026). This work was primarily supported by the CNOOC Key Laboratory of Liquefied Natural Gas and Low-Carbon Technology.

Conflicts of Interest: Xinyue Lu, Feng Chen, Fang Liu, Ruiying Chen, Xiaxue Jiang, Dongyu An, and Hairui Liang are employees of the same subsidiary of China National Offshore Oil Corporation. This study received no corporate funding. This work was supported by the National Natural Science Foundation of China (52676150, 52674126 and 52304098), the Natural Science Foundation of Guangdong Province (2025A1515010748), the State Key Laboratory of Intelligent Construction and Healthy Operation and Maintenance of Deep Underground Engineering (SDQZK2631), and the Youth Science and Technology Talent Support Programme of the Guangdong Provincial Association for Science and Technology. Apart from the relationships and funding disclosed above, the authors declare no other competing interests.

References

1. Li, H. CO_2 capture by various nanoparticles: Recent development and prospective. *J. Clean. Prod.* **2023**, *414*, 137679. [CrossRef]
2. Mon, M.T.; Tansuchat, R.; Yamaka, W. CCUS Technology and Carbon Emissions: Evidence from the United States. *Energies* **2024**, *17*, 1748. [CrossRef]
3. Dou, L.; Sun, L.; Lyu, W.; Wang, M.; Gao, F.; Gao, M.; Jiang, H. Trend of global carbon dioxide capture, utilization and storage industry and challenges and countermeasures in China. *Pet. Explor. Dev.* **2023**, *50*, 1246–1260. [CrossRef]
4. Huang, Y.; Liu, W.; Zhang, Y.X.; Zhang, X.J.; Wang, T.; Fang, M.X.; Yao, Y.L.; Zheng, X.; Liu, X.Y.; Jiang, L. Post-combustion absorption carbon capture assisted by sorption-compression cascade heat pump. *Carbon Capture Sci. Technol.* **2025**, *15*, 100393. [CrossRef]
5. Huang, Y.; Liu, W.; Zhang, X.J.; Wang, T.; Fang, M.X.; Gonzalez-Diaz, A.; Jiang, L. Flexibility analysis on absorption-based carbon capture integrated with energy storage. *Fuel* **2024**, *372*, 132279. [CrossRef]
6. Meng, L.; Kai, T.; Nakao, S.-I.; Yogo, K. Modeling of pre-combustion carbon capture with CO_2-selective polymer membranes. *Int. J. Greenh. Gas. Control* **2023**, *123*, 103830. [CrossRef]
7. Li, F.; Bai, Y.; Zeng, S.; Liang, X.; Wang, H.; Huo, F.; Zhang, X. Protic ionic liquids with low viscosity for efficient and reversible capture of carbon dioxide. *Int. J. Greenh. Gas. Control* **2019**, *90*, 102801. [CrossRef]
8. Berstad, D.; Anantharaman, R.; Nekså, P. Low-temperature CO_2 capture technologies–Applications and potential. *Int. J. Refrig.* **2013**, *36*, 1403–1416. [CrossRef]
9. Chen, C.; Zhang, S.; Row, K.H.; Ahn, W.-S. Amine–silica composites for CO_2 capture: A short review. *J. Energy Chem.* **2017**, *26*, 868–880. [CrossRef]
10. Sinehbaghizadeh, S.; Saptoro, A.; Mohammadi, A.H. CO_2 hydrate properties and applications: A state of the art. *Prog. Energy Combust. Sci.* **2022**, *93*, 101026. [CrossRef]
11. Ma, Z.W.; Zhang, P.; Bao, H.S.; Deng, S. Review of fundamental properties of CO_2 hydrates and CO_2 capture and separation using hydration method. *Renew. Sustain. Energy Rev.* **2016**, *53*, 1273–1302. [CrossRef]
12. Wang, P.; Li, Y.; Sun, N.; Han, S.; Wang, X.; Su, Q.; Li, Y.; He, J.; Yu, X.; Du, S.; et al. Hydrate Technologies for CO_2 Capture and Sequestration: Status and Perspectives. *Chem. Rev.* **2024**, *124*, 10363–10385. [CrossRef] [PubMed]
13. Majid, A.A.A.; Worley, J.; Koh, C.A. Thermodynamic and Kinetic Promoters for Gas Hydrate Technological Applications. *Energy Fuels* **2021**, *35*, 19288–19301. [CrossRef]
14. Liu, Z.; Liu, X.; Yang, M.; Pang, W.; Dou, B.; Song, Y. Thermodynamic and kinetic properties of gas hydrate phase transition from formation to decomposition with applications: A review. *J. Environ. Chem. Eng.* **2024**, *12*, 114614. [CrossRef]
15. Li, A.; Wang, J.; Bao, B. High-efficiency CO_2 capture and separation based on hydrate technology: A review. *Greenh. Gases Sci. Technol.* **2019**, *9*, 175–193. [CrossRef]
16. Ma, S.; Tian, X.; Liu, Z.; Wu, Z.; Li, G.; Guan, X.; Zheng, J.-N.; Yang, M. Formation and decomposition characteristics of CO_2+TBAB hydrate for a safer CO_2 storage. *Energy* **2024**, *307*, 132801. [CrossRef]
17. Lee, J.; Kim, K.-S.; Seo, Y. Thermodynamic, structural, and kinetic studies of cyclopentane + CO_2 hydrates: Applications for desalination and CO_2 capture. *Chem. Eng. J.* **2019**, *375*, 121974. [CrossRef]
18. Ge, B.-B.; Zhong, D.-L.; Lu, Y.-Y.; Li, X.-Y. Investigation of Tetrahydrofuran-CH_4 Hydrate Formation in Unstirred Conditions from a Different Perspective: Application to Solidified Natural Gas Storage. *Energy Fuels* **2023**, *37*, 15647–15656. [CrossRef]
19. Aliabadi, M.; Rasoolzadeh, A.; Esmaeilzadeh, F.; Alamdari, A. Experimental study of using CuO nanoparticles as a methane hydrate promoter. *J. Nat. Gas. Sci. Eng.* **2015**, *27*, 1518–1522. [CrossRef]
20. Li, D.; Lu, T.; Yu, Z.; Song, W.; Ding, Y.; Li, Y. Experimental investigation on the promotion of CO_2 hydrate formation for cold thermal energy storage–Effect of gas-inducing stirring under different agitation speeds. *Green Energy Resour.* **2023**, *1*, 100047. [CrossRef]

21. Xie, Y.; Zhu, Y.; Zheng, T.; Pan, H.; Sun, C.; Feng, J.; Chen, X.; Xu, L.; Wang, B.; Chen, G. Increase in Subcooling Elevates the SDS Concentration Threshold for Significantly Promoting CH_4 and CO_2 Hydrate Formation. *Ind. Eng. Chem. Res.* **2025**, *64*, 13161–13172. [CrossRef]
22. Liu, N.; Zhu, H.; Zhou, J.; Yang, L.; Liu, D. Molecular dynamics simulations on formation of CO_2 hydrate in the presence of metal particles. *J. Mol. Liq.* **2021**, *331*, 115793. [CrossRef]
23. Zhang, X.; Shan, T.; Song, H.; Li, J.; Wu, Q. Molecular dynamics study of the micro-mechanism of CO_2 hydrate formation in the confined space of porous media. *Int. J. Heat Mass Transf.* **2025**, *244*, 126940. [CrossRef]
24. Zatsepina, O.Y.; Buffett, B.A. Nucleation of CO_2-hydrate in a porous medium. *Fluid Phase Equilib.* **2002**, *200*, 263–275. [CrossRef]
25. Wu, L.-M.; Li, X.-Y.; Xie, F.-M.; Zhong, D.-L.; Englezos, P.; Yan, J. Minireview of Hydrate-Based CO_2 Separation from a CO_2/CH_4 Gas Mixture: Progress and Outlook. *Energy Fuels* **2022**, *36*, 10478–10488. [CrossRef]
26. Yang, M.; Song, Y.; Ruan, X.; Liu, Y.; Zhao, J.; Li, Q. Characteristics of CO_2 Hydrate Formation and Dissociation in Glass Beads and Silica Gel. *Energies* **2012**, *5*, 925–937. [CrossRef]
27. Masoomi, M.Y.; Morsali, A.; Dhakshinamoorthy, A.; Garcia, H. Mixed-Metal MOFs: Unique Opportunities in Metal–Organic Framework (MOF) Functionality and Design. *Angew. Chem. Int. Ed.* **2019**, *58*, 15188–15205. [CrossRef] [PubMed]
28. He, H.; Li, R.; Yang, Z.; Chai, L.; Jin, L.; Alhassan, S.I.; Ren, L.; Wang, H.; Huang, L. Preparation of MOFs and MOFs derived materials and their catalytic application in air pollution: A review. *Catal. Today* **2021**, *375*, 10–29. [CrossRef]
29. Duan, J.; Li, Q.; Fu, Y.; Chen, S.; Zhang, Y.; Liu, D. Accelerated formation of hydrate in size-varied ZIF-8 for CH_4 storage by adsorption-hydration hybrid technology. *Fuel* **2022**, *322*, 124266. [CrossRef]
30. Mu, L.; Liu, B.; Liu, H.; Yang, Y.; Sun, C.; Chen, G. A novel method to improve the gas storage capacity of ZIF-8. *J. Mater. Chem.* **2012**, *22*, 12246–12252. [CrossRef]
31. Kim, D.; Ahn, Y.-H.; Lee, H. Phase Equilibria of CO_2 and CH_4 Hydrates in Intergranular Meso/Macro Pores of MIL-53 Metal Organic Framework. *J. Chem. Eng. Data* **2015**, *60*, 2178–2185. [CrossRef]
32. Liu, X.; Chen, H.; Yuan, J.; Li, X.; Yu, J. Evaluation and screening of metal-organic frameworks for the adsorption and separation of methane and hydrogen. *Mater. Today Commun.* **2022**, *33*, 104602. [CrossRef]
33. Song, B.; Liang, Y.; Zhou, Y.; Zhang, L.; Li, H.; Zhu, N.-X.; Tang, B.Z.; Zhao, D.; Liu, B. CO_2-Based Stable Porous Metal–Organic Frameworks for CO_2 Utilization. *J. Am. Chem. Soc.* **2024**, *146*, 14835–14843. [CrossRef] [PubMed]
34. Zhao, T.; Nie, S.; Luo, M.; Xiao, P.; Zou, M.; Chen, Y. Research progress in structural regulation and applications of HKUST-1 and HKUST-1 based materials. *J. Alloys Compd.* **2024**, *974*, 172897. [CrossRef]
35. Jeong, N.C.; Samanta, B.; Lee, C.Y.; Farha, O.K.; Hupp, J.T. Coordination-Chemistry Control of Proton Conductivity in the Iconic Metal–Organic Framework Material HKUST-1. *J. Am. Chem. Soc.* **2012**, *134*, 51–54. [CrossRef] [PubMed]
36. Venna, S.R.; Jasinski, J.B.; Carreon, M.A. Structural Evolution of Zeolitic Imidazolate Framework-8. *J. Am. Chem. Soc.* **2010**, *132*, 18030–18033. [CrossRef] [PubMed]
37. Wang, P.; Li, K.; Yang, J.; Zhu, J.; Zhao, Y.; Teng, Y. Experimental and Theoretical Study on Dissociation Thermodynamics and Kinetics of Hydrogen-Propane Hydrate. *Chem. Eng. J.* **2021**, *426*, 131279. [CrossRef]
38. Kowalczyk, P.; Terzyk, A.P.; Gauden, P.A.; Solarz, L. Numerical analysis of Horvath–Kawazoe equation. *Comput. Chem.* **2002**, *26*, 125–130. [CrossRef] [PubMed]
39. Chen, Y.; Mu, X.; Lester, E.; Wu, T. High efficiency synthesis of HKUST-1 under mild conditions with high BET surface area and CO_2 uptake capacity. *Prog. Nat. Sci. Mater. Int.* **2018**, *28*, 584–589. [CrossRef]
40. Deng, J.; Jiang, H.; Liu, Y.; Yang, Y.; Luo, F.; Sun, B.; Chen, J.; Wang, C.; Tang, D.; Wen, T. Effect of ZIF-8 on Methane Hydrate Growth Kinetics in Oil–Water Systems. *Ind. Eng. Chem. Res.* **2024**, *63*, 2632–2641. [CrossRef]
41. Lv, X.; Bai, B.; Liang, S.; Zeng, W.; Liu, Y.; Ma, Q.; Zhang, H.; Wang, C.; Zhou, S. Study on the growth kinetics of methane hydrate in pure water system containing ZIF-8. *RSC Adv.* **2022**, *12*, 21203–21212. [CrossRef] [PubMed]
42. Ito, H.; Gibo, A.; Shiraishi, S.; Yasuda, K.; Ohmura, R. Renewed Measurements of Carbon Dioxide Hydrate Phase Equilibrium. *Int. J. Thermophys.* **2023**, *44*, 128. [CrossRef]
43. Álvarez, J.R.; Sánchez-González, E.; Pérez, E.; Schneider-Revueltas, E.; Martínez, A.; Tejeda-Cruz, A.; Islas-Jácome, A.; González-Zamora, E.; Ibarra, I.A. Structure stability of HKUST-1 towards water and ethanol and their effect on its CO_2 capture properties. *Dalton Trans.* **2017**, *46*, 9192–9200. [CrossRef] [PubMed]
44. Domán, A.; Czakkel, O.; Porcar, L.; Madarász, J.; Geissler, E.; László, K. Role of water molecules in the decomposition of HKUST-1: Evidence from adsorption, thermoanalytical, X-ray and neutron scattering measurements. *Appl. Surf. Sci.* **2019**, *480*, 138–147. [CrossRef]
45. Müller, K.; Vankova, N.; Schöttner, L.; Heine, T.; Heinke, L. Dissolving uptake-hindering surface defects in metal–organic frameworks. *Chem. Sci.* **2019**, *10*, 153–160. [CrossRef] [PubMed]

46. Liu, H.; Guo, P.; Regueira, T.; Wang, Z.; Du, J.; Chen, G. Irreversible Change of the Pore Structure of ZIF-8 in Carbon Dioxide Capture with Water Coexistence. *J. Phys. Chem. C* **2016**, *120*, 13287–13294. [CrossRef]
47. Zhang, S.; Fortier, H.; Dahn, J.R. Characterization of zinc carbonate hydroxides synthesized by precipitation from zinc acetate and potassium carbonate solutions. *Mater. Res. Bull.* **2004**, *39*, 1939–1948. [CrossRef]

Disclaimer/Publisher's Note: The statements, opinions and data contained in all publications are solely those of the individual author(s) and contributor(s) and not of MDPI and/or the editor(s). MDPI and/or the editor(s) disclaim responsibility for any injury to people or property resulting from any ideas, methods, instructions or products referred to in the content.